CrossMark

A Comparison Between Corrosion Behaviors of Fine-Grained and Coarse-Grained Structures of High-Mn Steel in NaCl Solution

M. Yeganeh, M. Eskandari, and S.R. Alavi-Zaree

In this study, a fine-grained structure was obtained in high-Mn austenitic steel through martensite treatment. The corrosion response of fine-grained and coarse-grained steels was studied and compared in 3.5 wt.% NaCl solution. Electrochemical impedance spectroscopy (EIS), potentiodynamic polarization, and Mott-Schottky analysis were performed to understand the effect of grain refinement on the electrochemical behavior of this steel. Microstructural evaluation showed that by reduction in grain size, the amount of low energy grain boundaries was increased, which led to better electrochemical behavior. In addition, the corrosion resistance of fine-grained steel did not deteriorate in comparison with coarse-grained steel. Both specimens showed a charge-transfer resistance of about 4-5 kΩ cm^2 in NaCl. Besides, a protective film related to fine-grained sample was detected by EIS and Mott-Schottky analysis, which could be a sign of higher grain boundaries in this steel.

1. Introduction

High-manganese (15-30 wt.%) steels such as transformation-induced plasticity (TRIP) and twinning-induced plasticity (TWIP) steels display excellent behavior in applications for structural components such as vehicle industry due to their exceptional combination of strength, crashworthiness, and ductility (Ref 1-6). There has been a growing interest in developing nano/ultrafine-grained steels in order to achieve higher strength without sacrificing ductility (Ref 7, 8). Although the mechanical response of Mn steels is excellent, the corrosion resistance of such steels is not significant (Ref 9, 10). The corrosion resistance of high-Mn steels may be improved by the addition of Al, Cr, and Si. There is little information in the literature on the electrochemical corrosion behavior of these steels, especially the fine-grained structures, in aqueous media (Ref 10, 13). Grajcar et al. (Ref 10) showed that the corrosion behavior of high-Mn steels is more affected by their chemical composition. It was also observed that high-Mn steels could show a tendency to passivation in corrosive media, probably due to the presence of alloying elements (Ref 11-14). For instance, Al, Cu, and Cr elements can form a

protective layer which leads to an increase in E_{corr} and a decrease in I_{corr} in H$_2$SO$_4$ solution (Ref 14-16).

In the previous work (Ref 17), it was shown that the formation of nano/fine-grained structure improved the mechanical properties of austenitic steels. However, increasing the volume fraction of grain boundaries due to grain refinement may degrade corrosion properties of steels. On the other hand, there are considerable reports (Ref 18-24) on improvement in corrosion properties of nano/fine-grained austenitic stainless steels compared with coarse-grained steel. In the present study, a fine-grained high-Mn steel was produced via a thermomechanical treatment called martensite treatment (Ref 20, 25, 26). The corrosion resistance of a high-Mn steel in both conditions of coarse-grained and fine-grained structures was investigated by electrochemical impedance spectroscopy, potentiodynamic polarization, and Mott-Schottky tests.

2. Experimental Procedure

2.1 Material

The experimental material was received as-hot-rolled condition with the chemical composition of Fe-0.07C-18Mn-2.00Si-2.00Al (wt.%). The hot-rolled microstructure consisted of 99.5% austenite phase with a grain size of 45 ± 5 μm. The mechanical behavior and detailed microstructures of the experimental steel have been reported elsewhere (Ref 1, 3). The actual martensite content was determined using a Ferriteoscope model MP30 and considering the following equation (Ref 26):

$$\text{Vol.\% martensite} = 1.75 \times \text{Ferriteoscope reading}$$

2.2 Martensite Treatment

In order to achieve a fine-grained structure, the martensite treatment was applied through compression deformation fol-

M. Yeganeh, Department of Materials Science and Engineering, Faculty of Engineering, Shahid Chamran University of Ahvaz, Ahvaz, Iran; **M. Eskandari** and **S.R. Alavi-Zaree**, Department of Materials Science and Engineering, Faculty of Engineering, Shahid Chamran University of Ahvaz, Ahvaz, Iran; and Steel Research Center, Faculty of Engineering, Shahid Chamran University of Ahvaz, Ahvaz, Iran. Contact e-mails: m.eskandari1362@gmail.com, m.eskandari@scu.ac.ir, and m.eskandari@ut.ac.ir.

lowed by annealing treatment. The compression specimen, with the diameter of 8 mm and the height of 12 mm, was machined from the hot-rolled plate along the rolling direction according to ASTM E209 standard. The compression test was carried out using a Gotech AI-7000 universal testing machine in the temperature of 25 °C under the constant strain rate of 0.01 s^{-1}. The specimen was compressed to a true strain of 0.6 followed by immediate water quenching in order to keep the deformed microstructures unchanged and prevent the formation of precipitations during air cooling. The deformed specimen was annealed at 750 °C for 300 s. In addition, the tint etching technique with picric acid in 100 mL ethanol and sodium metabisulfite was used.

2.3 Preparation for EBSD

The microstructural analysis was performed using a Hitachi SU6600 field emission scanning electron microscope (FE-SEM), equipped with a Nordlys Nano Oxford detector of electron backscattered diffraction (EBSD) which can operate at a voltage of 20 kV. The specimens were mechanically polished with SiC papers followed by electro-polishing to prevent formation of ά or ε-martensite during sample preparation. The patterns were acquired using the AZTEC 2.0 data acquisition software compatible with the EBSD detector with a binning of 4×4 pixels and a minimum of six bands for pattern recognition using acquisition rates (20 frames/s). The EBSD raw data were further analyzed using the Oxford Instruments Channel 5 post-processing software.

2.4 Texture Measurements

The texture measurement was carried out using a Bruker D8 diffractometer with Cr Ka radiation and a 2D Hi-star detector. To calculate the orientation distribution function (ODF), three pole figures were used for FCC austenite {(111), (200), (220)}. The measured pole figures were further treated with Resmat TexTools to calculate the inverse pole figures. Moreover, grain boundary character distribution analysis was obtained by post-processing using TexTools software.

2.5 Electrochemical Measurement

The corrosion performance was evaluated by open-circuit potential (E_{corr}) monitoring, potentiodynamic polarization, electrochemical impedance spectroscopy (EIS), and Mott-Schottky measurements in a 3.5 wt.%. NaCl solution. Electrochemical measurements were performed via an AUTOLAB PGSTAT 30 potentiostat controlled by NOVA software. A three conventional electrode cell was used to perform the electrochemical tests, with a platinum wire as a counter electrode and an Ag/AgCl electrode as the reference electrode. The chosen area of the working electrode (coarse-grained (CG) high-Mn steel and fine-grained (FG) high-Mn steel) was 0.1 cm^2. The polarization curves were performed in a potential range between −200 mV (below OCP—open-circuit potential) to 1000 mV (above OCP) with a scan rate of 1 mV/s. Corrosion rate (i_{corr}), corrosion potential (E_{corr}), and Tafel slopes were determined by NOVA software. For the EIS measurements, the amplitude of the EIS perturbation signal was set 5 mV sinusoidal (rms signal) and the frequency range was changed from 100 kHz to 10 mHz. Three replications were performed to ensure repeatability of the process. ZView 3.1c software was used to analyze EIS data. Mott-Schottky analysis was per-

formed at a frequency of 1 kHz using a 10 mV ac signal and a step potential of 25 mV in the cathodic direction form the initial potential of 0.9 V versus Ag/AgCl to the final potential of 0 V versus Ag/AgCl.

3. Results and Discussion

Figure 1 shows the initial austenite microstructure of the as-hot-rolled material. The material has a moderate grain size of 45 ± 5 μm with few annealing twinning. Figure 2 illustrates the tint-etched microstructure of the deformed specimen after straining to 0.6. As seen in this figure, the austenite grains are refined by strain-induced martensite phase. Detailed microstructural studies of this steel (Ref 1, 3) confirmed that both types of ε-martensite and ά-martensite were formed during room temperature deformation. The Ferriteoscope results showed that the volume fraction of ά-martensite reaches 85 pct after compression to 0.6. Austenitic-Mn steels contain thermodynamically metastable austenite at room temperature and are easily transformed into martensite. The fragmentation of martensite occurs during further deformation, and the martensite is reverted to austenite during subsequent annealing, leading to a noticeable grain refinement (Ref 26). The annealing microstructure of the deformed specimen at 750 °C for 300 s is shown in Fig. 3. As it can be seen in Fig. 3(a) and (b), a FG structure with an average grain size of 2.5 ± 0.5 μm was achieved as a result of martensite treatment and recrystallization process. The grain size distribution curve is shown in Fig. 3(c). The Ferriteoscope results confirmed that martensite phases were fully reverted to austenite phase during annealing. The coincidence site lattice (CSL) map of the annealed specimen is seen in Fig. 3(b). Moreover, sigma value distribution curve is indicated in Fig. 3(d). Among the CSL types, the volume fraction of $\Sigma 3$ boundary is dominant. It was well established that CSL boundaries are developed during annealing treatment in austenitic steels (Ref 27).

Figure 4 displays the macro-texture of the annealed specimen obtained by x-ray diffraction technique. As is seen in inverse pole figure, the as-received CG specimen depicted a weak texture. Likewise, a weak texture in the FG specimen was obtained after martensite treatment.
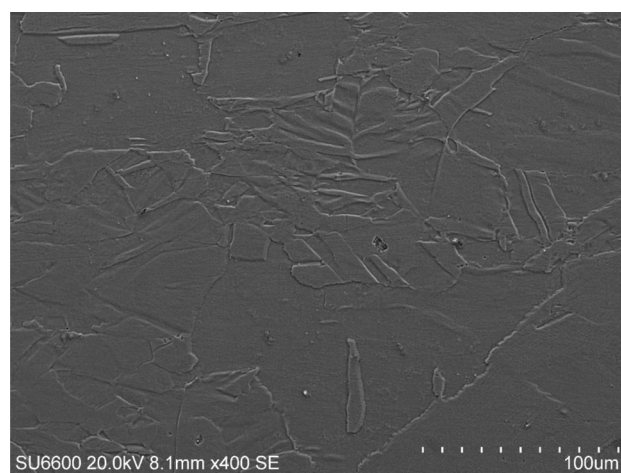

Fig. 1 Initial microstructure of hot-rolled specimen

Considering the CSL map of the FG specimen shown in Fig. 3(b) and (d), it can be speculated that grain boundaries with misorientation angles close to 60° may be related to Σ3. It

Fig. 2 Tint-etched microstructure of deformed specimen to 60 pct

has been reported that in some face-centered cubic steels with low stacking fault energy, such as austenitic stainless steels, the frequency of low Σ CSL grain boundaries can be significantly increased using appropriate thermo-mechanical treatments (Ref 27-30).

Figure 5 shows the Nyquist curve for the CG and the FG specimens in 3.5 wt.%. NaCl. The equivalent model shown in this figure includes the solution resistance R_s, the charge-transfer resistance R_{ct}, and the constant phase element CPE_{ct}, which is a non-ideal capacitor in the metal-solution interface. The theoretical impedance value of a CPE is equal to $A^{-1} (i\omega)^{-n}$, where A is a constant corresponding to the interfacial capacitance, i is the imaginary number, ω is the angular frequency, and n is an exponential factor in the range of -1 and 1 (Ref 31). The optimized values for circuits parameters obtained from ZView 3.1c software are summarized in Table 1. The charge-transfer resistances of the CG and the FG specimens in the NaCl solution were obtained to be 4190 and 5000 Ω cm^2, respectively. Besides, the CPE_{ct} values for the CG and the FG specimens were calculated to be 28×10^{-5} and 23×10^{-5} F/cm^2, respectively. These results showed that grain refinement led to a slight better corrosion resistance in the FG compared with the CG specimen in the NaCl solution.
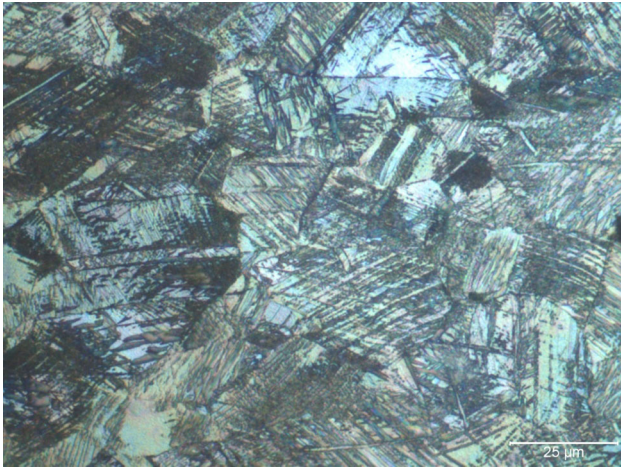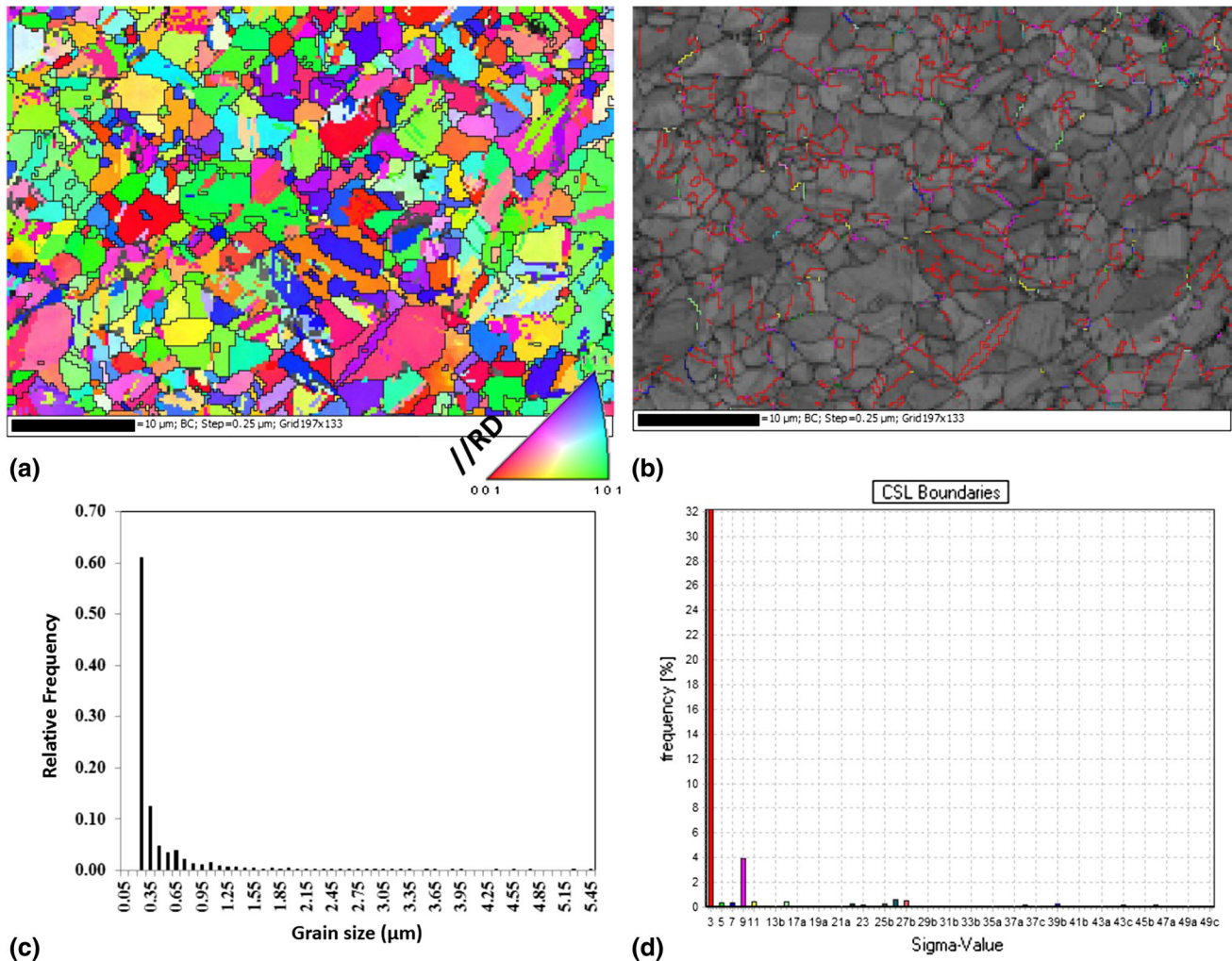

Fig. 3 Microstructure of annealed specimen at 750 °C after 300 s: (a) orientation map of austenite phase, (b) band contrast showing coincidence site lattice (Σ3 as red, Σ9 as pink and Σ11 as yellow), (c) grain size distribution obtained by EBSD, (d) sigma value distribution (Color figure online)
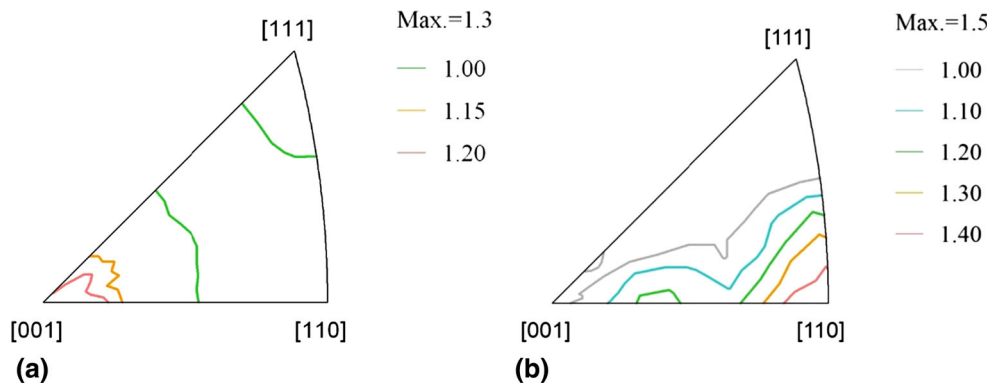
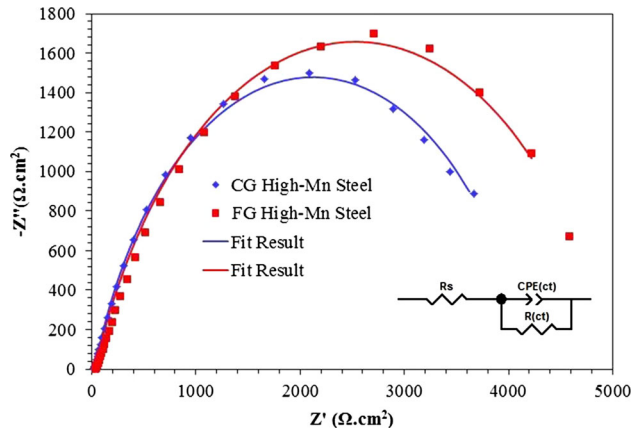**Fig. 4** Macro-texture analysis of (a) as-received CG specimen, (b) FG specimen

Fig. 5 Nyquist plots for CG and FG specimens in 3.5 wt.% NaCl solution

Table 1 Impedance data obtained by ZView simulation for CG and UFG high-Mn steels in 3.5 wt.% NaCl solution

Sample	R_s, Ω cm^2	R_{ct}, Ω cm^2	CPE$_{ct}$, F/cm^2	n
CG	30	4190	28×10^{-5}	0.78
UFG	30.3	5000	23×10^{-5}	0.74

Figure 6 shows bode and phase diagrams related to the corrosion resistance of the CG and the FG steels in the NaCl solution. The bode diagram showed higher values of impedance modulus $|Z|\left(\left[Z'^2 + Z''^2\right]^{1/2}\right)$ for the FG at higher frequencies in comparison with the CG specimen. High frequency region in the EIS curves was associated to the capacitance response corresponding to the thin oxide layer or increment of Σ CSL grain boundaries after the thermo-mechanical treatment. By increasing Σ CSL of grain boundaries for the FG sample, it could be concluded that the susceptibility in the corrosive media was decreased and the high energy borders were reduced. It may be concluded that the higher values of $|Z|$ in the high frequency region corresponding the FG steel was a sign of grain boundaries variation due to the thermo-mechanical process. Therefore, the FG steel showed higher impedance modulus in the high frequency region. Besides, the phase angle diagram obtained for the FG steel showed higher contents at higher frequencies, which could be a sign of greater resistance in this region (Ref 32).

Figure 7 depicts potentiodynamic polarization behavior of the CG and the FG steels after immersing in a 3.5 wt.%. NaCl. Table 2 illustrates the amount of I_{corr}, E_{corr}, and Tafel slope lines (β_a and β_c). I_{corr} associated to the CG and the FG steels were obtained 2 and 4 μA/cm^2, respectively. The corrosion current density of these two steels was in the same range, which was also observed by the EIS data. However, in the anodic sweep, the FG steel showed a lower current density. This could

be due to the higher corrosion resistance of the FG steel due to the development of CSL boundaries, which was emphasized by the EIS plots. Finally, at high anodic potentials, the FG and the CG steels indicated the same behavior, more likely due to the highly deterioration of oxide layer in the FG steel. It should be mentioned that a shift to more noble potentials, as presented in Fig. 7, could be related to the presence of an alloying element such as Al which has the tendency toward passivation (Ref 15). In steels, Mn forms unstable manganese oxide due to low passivity coefficient and hence reduces their electrochemical corrosion resistances. Mn oxide precipitates in the passive film, and therefore, the resistance to the pitting corrosion is decreased (Ref 15). On the other hand, Al passivity coefficient is much greater than that of Mn. Hence, adding Al to steel is expected to promote the passivation ability via forming a compact Al_2O_3 film. In a chloride-containing solution (near neutral pH), whereas Al forms a protective Al_2O_3 oxide film (Ref 15, 33), Si forms a silica film in acidic pH, where TWIP steel exposes high corrosion in the acidic environment due to the poor passivation tendency of Al and high dissolution of Mn and Fe (Ref 13). Thermodynamically, Al_2O_3 and SiO_2 are very stable with respect to the metal and have high melting points. Also, their transport processes through the scales are generally slow (Ref 34).

Figure 8 displays the Mott-Schottky plots for the passive films formed on the CG and the FG high-Mn steels in 3.5 wt.% NaCl. According to the Mott-Schottky theory, the space charge capacitances of n-type semiconductor were given by Eq 1 (Ref 35, 36):

$$\frac{1}{C^2} = \frac{2}{\varepsilon\varepsilon_0 eN_D}\left(E - E_{fb} - \frac{kT}{e}\right) \qquad \text{(Eq 1)}$$

where e is the electron charge (1.602×10^{-19} C), N_D is the donor density for n-type semiconductor, ε is the dielectric constant of the passive film, usually taken as 15.6 (Ref 37), ε_0 is the vacuum permittivity (8.854×10^{-14} F/cm), k is the
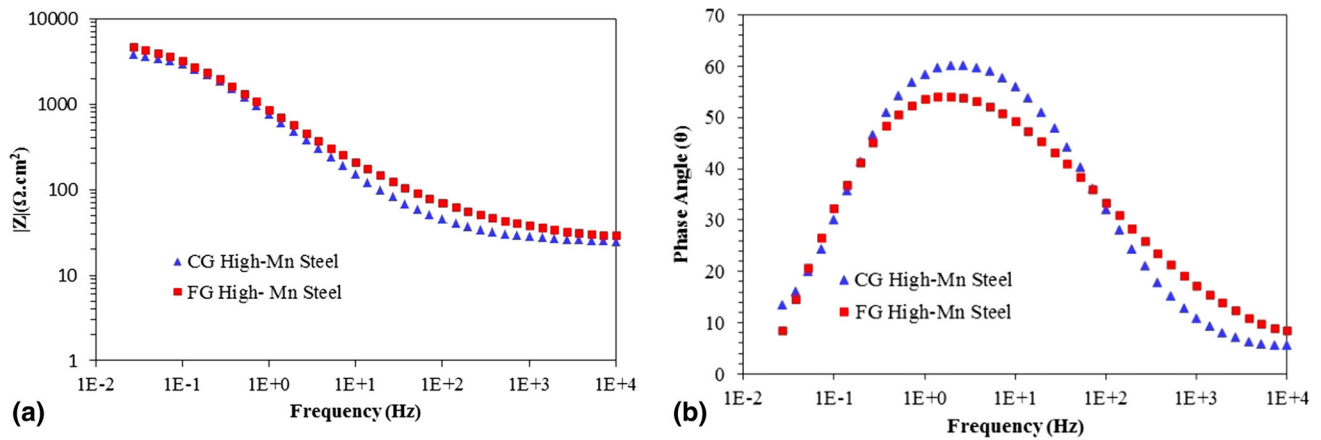
Fig. 6 Bode (left) and phase (right) diagrams plots for CG and FG specimens in 3.5 wt.% NaCl solution
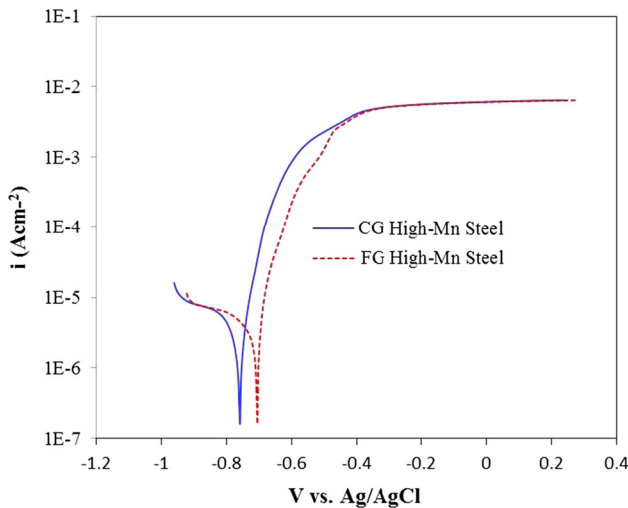

Fig. 7 Potentiodyamic polarization of CG and FG specimens in 3.5 wt.% NaCl

Boltzmann constant (1.38×10^{23} J/K), T is the absolute temperature, and E_{fb} is the flat band potential. The term kT/e is neglected because it is only about 25 mV at room temperature. In Eq 1, N_D can be calculated from the slope of the experimental C^{-2} versus E plots, and E_{fb} from the extrapolation of the linear portion to $C^{-2} = 0$ (Ref 37). N_D is calculated from $N_D = \frac{2}{\varepsilon \varepsilon_0 eS}$, where S is the slope of the experimental C^{-2} versus E plot (Ref 38). For a p-type semiconductor, C^{-2} versus E should be linear with a negative slope which is inversely proportional to the acceptor density. On the other hand, an n-type semiconductor yields a positive slope which is inversely proportional to the donor density (Ref 37). As is observed in Fig. 8, both samples show positive slopes indicating the presence of n-type semiconductor on the surface. This type of semiconductor could be due to the combination of a metal oxide like Fe_2O_3 (Ref 39) and MnO_2 (Ref 40) or oxygen vacancies (Ref 41). Moreover, the N_D calculated for the CG and the FG high-Mn steels was about 9×10^{21} and 11×10^{21} cm^{-3}, respectively. Therefore, the donor densities of the passive-like film formed on the FG steel was higher than that of the CG steel, which can be attributed to the higher grain boundary defects of the FG sample. The increase in the linear slope at the transition potential

Table 2 Corrosion parameters of CG and UFG steel in 3.5 wt.% NaCl

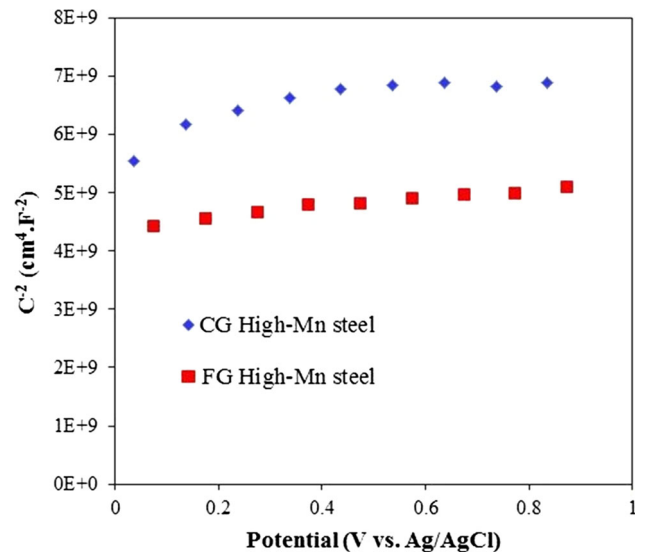| Sample	I_{corr}, μA/cm^2	E_{corr}, mV versus Ag/AgCl	β_a, mV/dec	β_c, mV/dec
CG	2	−760	105	40
UFG	4	−710	97	67

Fig. 8 Mott-Schottky plots related to CG and FG specimens in 3.5 wt.% NaCl

implies that the donor density of the passive film was decreased because the donor density was inversely proportional to the slope (Ref 41).

As mentioned earlier in Fig. 3, by applying a thermo-mechanical process on high-Mn steel, low Σ CSL (lower energy boundaries) was obtained in the FG specimen. The formation of CSL boundary may lead to lower susceptibility to corrosion damages in the FG sample. Indeed, based on the electrochemical tests conducted, the researchers observed that the thermo-mechanical process and the increment in the number

of grain boundaries in the FG sample could not deteriorate the corrosion behavior of high-Mn steel in the NaCl solution.

4. Conclusions

In the present work, the corrosion resistance of the FG and the CG high-Mn steels was investigated and compared in 3.5 wt.% NaCl solution and the following main characteristics were found:

1. A FG specimen with a weak texture was obtained as a result of martensite treatment in present high-Mn steel.
2. The FG high-Mn steel showed high volume fraction of $\Sigma 3$ boundary due to the thermo-mechanical process.
3. The calculated i_{corr} and R_{ct} for both the CG and the FG high-Mn steels were relatively identical, which demonstrated increment in grain boundaries could not influence corrosion resistance.
4. The obtained N_D for the FG sample was higher than the CG one. It might be due to easier diffusion of oxygen atoms through the surface.
5. Corrosion resistance of the FG specimen did not degrade in comparison with CG specimen due to the presence of CSL boundaries.

References

1. M. Eskandari, A. Zarei-Hanzaki, M.A. Mohtadi-Bonab, Y. Onuki, R. Basu, A. Asghari, and J.A. Szpunar, Grain-Orientation-Dependent of γ-ε-α' Transformation and Twinning in a Super-High-Strength, High Ductility Austenitic Mn-Steel, *Mater. Sci. Eng., A*, 2016, **674**, p 514–528
2. M. Eskandari, M.R. Yadegari-Dehnavi, A. Zarei-Hanzaki, M.A. Mohtadi-Bonab, R. Basu, and J.A. Szpunar, In-Situ Strain Localization Analysis in Low Density Transformation-Twinning Induced Plasticity Steel Using Digital Image Correlation, *Opt. Laser Eng.*, 2015, **67**, p 1–16
3. M. Eskandari, A. Zarei-Hanzaki, J.A. Szpunar, M.A. Mohtadi-Bonab, A.R. Kamali, and M. Nazarian-Samani, Microstructure Evolution and Mechanical Behavior of a New Microalloyed High Mn Austenitic Steel During Compressive Deformation, *Mater. Sci. Eng., A*, 2014, **615**, p 424–435
4. O. Bouaziz, S. Allain, C.P. Scott, P. Cugy, and D. Barbier, High Manganese Austenitic Twinning Induced Plasticity Steels: A Review of the Microstructure Properties Relationships, *Curr. Opin. Solid State Mater. Sci.*, 2011, **15**, p 141–168
5. G. Frommeyer, U. Brux, and P. Neumann, Supra-Ductile and High-Strength Manganese-TRIP/TWIP Steels for High Energy Absorption Purposes, *ISIJ Int.*, 2003, **43**, p 438–442
6. I. Gutierrez-Urruti and D. Raabe, Influence of Al Content and Precipitation State on the Mechanical Behavior of Austenitic High-Mn Low-Density Steels, *Scr. Mater.*, 2013, **68**, p 343–347
7. R.D.K. Misra, B.R. Kumar, and M. Somani, Deformation Processes During Tensile Straining of Fine/Nanograined Steel by Reversion in Metastable Austenitic Steel, *Scr. Mater.*, 2008, **59**, p 79–82
8. D.L. Johnnsen, A. Kyrolainen, and P.J. Ferreira, Influence of Annealing Treatment on the Formation of Nano/Submicron Grain Size AISI, 301 Austenitic Stainless Steels, *Metall. Trans. A*, 2006, **37**, p 2325–2338
9. M. Khalissi, R.K.S. Raman, and S. Khoddam, Stress Corrosion Cracking of Novel Steel for Automotive Applications, *Procedia Eng.*, 2011, **10**, p 3381–3386
10. A. Grajcar, M. Kciuk, S. Topolska, and A. Płachcinska, Microstructure and Corrosion Behavior of Hot-Deformed and Cold-Strained High-Mn Steels, *J. Mater. Eng. Perform.*, 2016, **25**, p 2245–2254
11. V.F.C. Lins, M.A. Freitas, and E.M.P. Silva, Corrosion Resistance Study of Fe-Mn-Al-C Alloys Using Immersion and Potentiostatic Tests, *Appl. Surf. Sci.*, 2005, **250**, p 124–134
12. M.B. Kannan, R.K. Singh Raman, and S. Khoddam, Comparative Studies on the Corrosion Properties of a Fe-Mn-Al-Si Steel and an Interstitial-Free Steel, *Corros. Sci.*, 2008, **50**, p 2879–2884
13. M. Bobby-Kannan, R.K. Singh-Raman, S. Khoddam, and S. Liyanaarachchi, Corrosion Behavior of Twinning-Induced Plasticity (TWIP) Steel, *Mater. Corros.*, 2011, **61**, p 1–5
14. Y.S. Zhang, X.M. Zhu, and S.H. Zhong, Effect of Alloying Elements on the Electrochemical Polarization Behavior and Passive Film of Fe-Mn Base Alloys in Various Aqueous Solutions, *Corros. Sci.*, 2004, **46**, p 853–876
15. Y.S. Zhang and X.M. Zhu, Electrochemical Polarization and Passive Film Analysis of Austenitic Fe-Mn-Al Steels in Aqueous Solutions, *Corros. Sci.*, 1999, **41**, p 1817–1833
16. T. Dieudonné, L. Marchetti, M. Wery, F. Miserque, M. Tabarant, J. Chêne, C. Allely, P. Cugy, and C.P. Scot, Role of Copper and Aluminum on the Corrosion Behavior of Austenitic Fe-Mn-C TWIP Steels in Aqueous Solutions and the Related Hydrogen Absorption, *Corros. Sci.*, 2014, **83**, p 234–244
17. K.D. Ralston and N. Birbilis, Effect of Grain Size on Corrosion: A Review, *Corrosion*, 2010, **66**(7), p 1–13
18. M. Pisarek, P. Kedzierzawski, M. Janik-Czachor, and K.J. Kurzydlowski, Effect of Hydrostatic Extrusion on Passivity Breakdown on 303 Austenitic Stainless Steel in Chloride Solution, *J. Solid State Electrochem.*, 2009, **13**, p 283–291
19. A.D. Schino, M. Barteri, and J.M. Kenny, Grain Size Dependence of Mechanical, Corrosion and Tribological Properties of High Nitrogen Stainless Steels, *J. Mater. Sci.*, 2003, **38**, p 3257–3262
20. L. Jinlong and L. Hongyun, Effect of Temperature and Chloride Ion Concentration on Corrosion of Passive Films on Nano/Ultrafine Grained Stainless Steels, *J. Mater. Eng. Perform.*, 2014, **23**, p 4223–4229
21. A.T. Krawczynska, M. GlocK, and K. Lublinska, Intergranular Corrosion Resistance of Nanostructured Austenitic Stainless Steel, *J. Mater. Sci.*, 2013, **48**, p 4517–4523
22. R.K. Wang, Z.J. Zheng, and Y. Gao, Effect of Shot Peening on the Intergranular Corrosion Susceptibility of a Novel Super 304H Austenitic Stainless Steel, *J. Mater. Eng. Perform.*, 2016, **25**, p 20–28
23. Z.J. Zheng, Y. Gao, Y. Gui, and M. Zhu, Corrosion Behaviour of Nanocrystalline 304 Stainless Steel Prepared by Equal Channel Angular Pressing, *Corros. Sci.*, 2012, **54**, p 60–67
24. X.Y. Wang and D.Y. Li, Mechanical and Electrochemical Behavior of Nanocrystalline Surface of 304 Stainless Steel, *Electrochim. Acta*, 2002, **47**, p 3939–3947
25. M. Eskandari, A. Kermanpur, and A. Najafizadeh, Formation of Nano-Grained Structure in a 301 Stainless Steel Using a Repetitive Thermo-Mechanical Treatment, *Mater. Letter*, 2009, **63**, p 1442–1444
26. M. Eskandari, A. Najafizadeh, and A. Kermanpur, Effect of Strain-Induced Martensite on the Formation of Nanocrystalline 316L Stainless Steel after Cold Rolling and Annealing, *Mater. Sci. Eng., A*, 2009, **519**, p 46–50
27. C. Hu, S. Xia, H. Li, T. Liu, B. Zhou, W. Chen, and N. Wang, Improving the Intergranular Corrosion Resistance of 304 Stainless Steel by Grain Boundary Network Control, *Corros. Sci.*, 2011, **53**, p 1880–1886
28. S. Xia, B. Zhou, and W. Chen, Grain Cluster Microstructure and Grain Boundary Character Distribution in Alloy 690, *Metall. Mater. Trans. A*, 2009, **40A**, p 3016–3030
29. S. Kobayashi, S. Tsurekawa, T. Watanabe, and G. Palumbo, Grain Boundary Engineering for Control of Sulfur Segregation Induced Embrittlement in Ultrafine-Grained Nickel, *Scr. Mater.*, 2010, **62**, p 294–297
30. S. Xia, B. Zhou, W. Chen, X. Luo, and H. Li, Features of Highly Twinned Microstructures Produced by GBE in FCC Materials, *Mater. Sci. Forum*, 2010, **638-642**, p 2870–2875
31. M. Saremi and M. Yeganeh, Application of Mesoporous Silica Nanocontainers as Smart Host of Corrosion Inhibitor in Polypyrrole Coatings, *Corros. Sci.*, 2014, **86**, p 159–170

32. M. Yeganeh and M. Saremi, The Effect of Mesoporous Silica Nanocontainers Incorporation on the Corrosion Behavior of Scratched Polymer Coatings, *Prog. Org. Coat.*, 2016, **90**, p 296–303

33. X.M. Zhu and Y.S. Zhang, Investigation of the Electrochemical Corrosion Behavior and Passive Film for Fe-Mn, Fe-Mn-Al, and Fe-Mn-Al-Cr Alloys in Aqueous Solutions, *Corrosion*, 1998, **54**, p 3–12

34. F.H. Stott, G.C. Wood, and J. Stringer, The Influence of Alloying Elements on the Development and Maintenance of Protective Scales, *Oxid. Met.*, 1995, **44**, p 113–145

35. N.B. Hakiki, S. Boudin, B. Rondot, and M.D.C. Belo, The Electronic Structure of Passive Films Formed on Stainless Steels, *Corros. Sci.*, 1995, **37**, p 1809–1822

36. Z. Feng, X. Cheng, C. Dong, L. Xu, and X. Li, Passivity of 316L Stainless Steel in Borate Buffer Solution Studied by Mott-Schottky Analysis, Atomic Absorption Spectrometry and X-ray Photoelectron Spectroscopy, *Corros. Sci.*, 2010, **52**, p 3646–3653

37. A. Fattah-alhosseini, M.A. Golozar, A. Saatchi, and K. Raeissi, Effect of Solution Concentration on Semiconducting Properties of Passive Films Formed on Austenitic Stainless Steels, *Corros. Sci.*, 2010, **52**, p 205–209

38. A.M.P. Simoes, M.G.S. Ferreira, B. Rondot, and M.C. Belo, Study of Passive Films Formed on AISI, 304 Stainless Steel by Impedance Measurements and Photoelectrochemistry, *J. Electrochem. Soc.*, 1990, **137**, p 82–87

39. A. Fattah-alhosseini and S. Vafaeian, Comparison of Electrochemical Behavior Between Coarse-Grained and Fine-Grained AISI, 430 Ferritic Stainless Steel by Mott-Schottky Analysis and EIS Measurements, *J. Alloy. Compd.*, 2015, **639**, p 301–307

40. A.H. Al-Falahi, Structural and Optical Properties of MnO_2: Pb Nanocrystalline Thin Films Deposited by Chemical Spray Pyrolysis, *IOSR. J. Eng.*, 2013, **3**, p 52–57

41. G.A. Zhang and Y.F. Cheng, Micro-electrochemical Characterization and Mott-Schottky Analysis of Corrosion of Welded X70 Pipeline Steel in Carbonate/Bicarbonate Solution, *Electrochim. Acta*, 2009, **55**, p 316–324